Carrier Transport Enhancement Mechanism in Highly Efficient Antimony Selenide Thin-Film Solar Cell

Yandi Luo, Guojie Chen, Shuo Chen, Nafees Ahmad, Muhammad Azam, Zhuanghao Zheng, Zhenghua Su, Michel Cathelinaud, Hongli Ma, Zhigang Chen, et al.

Carrier Transport Enhancement Mechanism in Highly Efficient Antimony Selenide Thin-Film Solar Cell

Yandi Luo, Guojie Chen, Shuo Chen, Nafees Ahmad, Muhammad Azam, Zhuanghao Zheng, Zhenghua Su, Michel Cathelinaud, Hongli Ma, Zhigang Chen, Ping Fan, Xianghua Zhang, and Guangxing Liang**

Y. Luo, G. Chen, S. Chen, N. Ahmad, Z. Zheng, Z. Su, P. Fan, G. Liang
Shenzhen Key Laboratory of Advanced Thin Films and Applications, Key Laboratory of Optoelectronic Devices and Systems of Ministry of Education and Guangdong Province, College of Physics and Optoelectronic Engineering, Shenzhen University
Shenzhen 518060, Guangdong, P. R. China
E-mail: lgx@szu.edu.cn (Prof. Liang) and chensh@szu.edu.cn (Prof. Chen)
Y. Luo, M. Cathelinaud, H. Ma, X. Zhang
CNRS, ISCR (Institut des Sciences Chimiques de Rennes) UMR 6226, Univ Rennes
Rennes F-35000, France
M. Azam
Department of Physics, Faculty of Sciences, University of Central Punjab Lahore, 54000, Pakistan
Z. Chen
School of Chemistry and Physics, Queensland University of Technology, Brisbane, Queensland 4001, Australia

Keywords: Sb_2Se_3 solar cells, heterojunction interface engineering, band alignment, carrier transport

Abstract

Exhibiting outstanding optoelectronic properties, antimony selenide (Sb_2Se_3) has attracted considerable interest and has been developed as a light absorber layer for thin-film solar cells over the decade. However, current state-of-the-art Sb_2Se_3 devices suffer from unsatisfactory "cliff-like" band alignment and severe interface recombination loss, which deteriorates device performance. In this work, the heterojunction interface of an Sb_2Se_3 solar cell is improved by introducing effective aluminum (Al^{3+}) cation into the CdS buffer layer. Then, the energy band alignment of Sb_2Se_3/CdS:Al heterojunction is modified from a "cliff-like" structure to a "spike-like" structure. Finally, heterojunction interface engineering suppresses recombination losses and strengthens carrier transport, resulting in a high efficiency of 8.41% for the substrate-structured Sb_2Se_3 solar cell. This work proposes a facile strategy for interfacial treatment and elucidates the related carrier transport enhancement mechanism, paving a bright avenue to overcome the efficiency bottleneck of Sb_2Se_3 thin-film solar cells.

1. Introduction

Considerable developments in thin-film solar cells in the past decades have facilitated the application of photovoltaic devices. [1-3] As a promising environment-friendly light-absorbing semiconductor material, antimony selenide (Sb_2Se_3) has attracted wide interest owing to its optoelectronic properties. Sb_2Se_3 thin film as a binary compound possesses high light absorption coefficient (greater than 10^5 cm^{-1}), suitable direct bandgap (about 1.17 eV), and begin carrier mobility (about 10 cm^2 V^{-1} s^{-1}).[4, 5] A single solar cell yields a maximum theoretical power conversion efficiency (PCE) above 30% originating from the Shockley–Queisser detail-balance model.[6] Covalently bonded $[Sb_4Se_6]_n$ ribbons are vertically stacked by van der Waals force interactions and form Sb_2Se_3 with a 1D crystal structure, exhibiting conspicuous anisotropic properties.[6, 7] Furthermore, high constituent abundance, low toxicity, cost-effectiveness, and simple fabrication process facilitate the application of high-efficiency thin-film solar cells in large-scale manufacturing. In recent years, remarkable progress has been made in the PCE of Sb_2Se_3-based photovoltaic devices. To date, the superior efficiency of 9.2% [8], 10.12% [5] and 10.57 % [9] for the core–shell-structured, substrate-structured and superstrate-structured Sb_2Se_3 thin-film solar cells were prepared through closed space sublimation (CSS), injection vapor deposition (IVD) and additive-assisted chemical bath deposition (CBD) method, respectively. Moreover, series connected antimony selenosulfide monolithic integrated photovoltaic modules have achieved PCE of 7.43% [10]. However, highest efficiency of Sb_2Se_3 thin-film solar cells remains considerably lower than the theoretical value and far inferior to that of the well-researched $CuInGaSe_2$ (CIGS) thin-film solar cells.[10]

In fact, several major affecting factors impede improvement in device efficiency, such as defects at the bulk and interface, the band alignment of heterojunction, and the device structure.[11] Particularly for the substrate-structured Sb_2Se_3 thin-film solar cells, the buffer layer and absorber layer characteristics play a critical role in a desirable heterojunction.[12] An excellent heterojunction is obviously favored for optimizing band alignment, and facilitating the generation, separation, and transportation efficiency of charge carriers, thereby enhancing the optoelectronic performance of devices.

According to previous works, [5, 13] CdS films are regarded as the most appreciable and effective buffer layers for high-quality heterojunctions in Sb_2Se_3 devices. However, some theoretical and experimental results pointed out that the main factor that deteriorates device performance is the high density of interfacial defects (about 10^{11} cm^{-3}) [14, 15] between Sb_2Se_3 and CdS. In addition, the unsatisfactory conduction band offset (CBO) at the Sb_2Se_3/CdS heterojunction was deemed a major limiting factor for device performance enhancement. A number of approaches, such as interfacial modification and element doping, have been used to improve heterojunction quality, enhance carrier transport, and suppress recombination. In this regard, incorporating doping elements, such as O,[16] K,[17] Zn,[18] and In,[19] presents a positive effect that optimizes the energy band alignment between Sb_2Se_3 and CdS. For example, it has demonstrated that the introduction of Zn could promote tuning interface band alignment and carrier transport, and thus the short-circuit current density was visibly enhanced.[18] The CdS:In buffer layer can effectively suppress charge recombination and result in efficient charge transport because of the enlarged bandgap.[19] In addition, doping O elements into the CdS buffer layer can effectively modify the band alignment from a "cliff-like" structure to a "spike-like" structure at the CdS:O/Sb_2Se_3 interface.[16] Thus, doping appropriate elements into the CdS layer can be considered as an effective approach for optimizing heterojunction quality and improving efficiency.

In this work, heterojunction quality and the performance of Sb_2Se_3 thin-film solar cell were efficiently enhanced by incorporating mild and low-cost Al^{3+} cations into the CdS buffer layer. The modified opto-electronic properties and corresponding improvement in the mechanism were systematically studied, and the effect of Al^{3+} doping on bandgap alignment tuning and carrier transport dynamics within Sb_2Se_3/CdS:Al solar cells were carefully investigated. Ultimately, the device achieved an outstanding efficiency of 8.41%, superior short-circuit current density (J_{SC}) of 28.26 mA/cm^2, open circuit voltage (V_{OC}) of 489 mV, and fill factor (FF) of 60.87 %, which was closely related to the suppression of defect-assisted recombination at the heterojunction interface, the optimization of band alignment with ideal CBO, and the enhancement of carrier transport efficiency. These interesting results highlight the vital potential for further

improvement of Sb_2Se_3 photovoltaic device efficiency and future practical application.

2. Results and discussion

An effective combination reaction **(Figure S1)** involving sputtering and selenization of Sb precursors was used in fabricating a Sb_2Se_3 thin film. The crystal structure of the Sb_2Se_3 thin film and crystal orientation and crystallinity were characterized through XRD analysis. The XRD pattern of the Sb_2Se_3 absorber layer is provided in **Figure S2 (a)**. Distinctly, the diffraction peaks of the as-prepared Sb_2Se_3 thin film matched well with the information provided by orthorhombic Sb_2Se_3 (JCPDS Card No. 15-0861) without any secondary phase, suggesting the absence of detectable impurities. As Sb_2Se_3 comprises covalently bond $[Sb_4Se_6]_n$ ribbons stacked by van der Waals force, an appropriate crystallographic orientation is critical to controlling the crystalline quality of Sb_2Se_3 thin films and their charge carrier transport ability.[20] Two prominent diffraction peaks: (221) and (211) demonstrated preferential crystallographic orientation along (hk1) of the Sb_2Se_3 thin film. Sb_2Se_3 crystal grains grown along the (hk1) orientation are conducive to the transport of photoexcited carriers. [12, 21] Thus, the as-fabricated Sb_2Se_3 thin film is theoretically a promising material that reduces interfacial recombination and improves device performance.

The SEM top-view image is shown in **Figure S2 (b)**. Highly crystalline, compact, and uniform characteristics were observed, along with the absence of visible voids on the surface. We analyzed the grain size distribution derived from the SEM image. The detailed frequency histogram versus Sb_2Se_3 grain size distribution is depicted in **Figure S2 (c)**. The average grain size was approximately 1.18 μm, which was equivalent to the thickness of the absorber layer, indicating effective restraining recombination losses resulting from the grain boundaries (GBs). Therefore, a high-quality Sb_2Se_3 absorber layer with preferred orientation, high crystallinity, compact, uniform, and large crystal grains was obtained and found to guarantee device performance.

Apart from the absorber layer, the buffer layer is a key factor for optimizing interface band alignment and improving device performance. Herein, the trivalent Al-doped CdS buffer layer was introduced to regulate band alignment and facilitate carrier transport

for Sb_2Se_3 thin-film solar cells. To evaluate the applicability potential of Al doping, various Al concentration-dependent Sb_2Se_3 thin-film solar cells were prepared with the substrate configuration of Mo/Sb_2Se_3/CdS:Al/ITO/Ag. Annealing treatment has been proven to be an indispensable factor in obtaining high-quality Al-doped CdS thin films.[2] An optimized annealing temperature of 280 °C and annealing time of 5 min can be verified through systematic investigation of the photovoltaic performance (**Figure S3 and S4**).

The detailed device performance parameters of Sb_2Se_3 device are summarized in **Table 1**, including various Al^{3+} doping concentrations (i.e., 0.1, 0.3, 0.5, and 0.7 M) and the counterparts of the pristine CdS-based sample, which were labeled as A1, A2, A3, A4, and A0. The Al-doped devices possessed an obvious increment in J_{SC} and showed improvement in PCE. The PCE revealed a gradual increase with increasing of Al concentration from 0.1 M to 0.5 M and then dramatically decreased under a high doping concentration of 0.7 M. These results indicated a strong correlation between cation doping concentration and device PCE.

The *J*–*V* curves of the representative A1, A3, and A0 devices under the standard AM 1.5 G light illumination are shown in **Figure 1(a)**. The A0 device presented a V_{OC} of 515 mV, FF of 57.62%, and J_{SC} of 22.98 mA/cm^2, thus achieving a PCE of 6.82%. By contrast, a competitive PCE of 8.41% was achieved for the A3 device, along with the major device parameters, that is, a V_{OC} of 489 mV and simultaneous increases in FF to 60.87% and J_{SC} to 28.26 mA/cm^2. To check the reproducibility of the devices, we prepared a set of 20 devices for each category. The statistical distributions of the key photovoltaic parameters of the representative devices are displayed in **Figure S5**. The acceptable performance variation within all single-category devices indicated the outstanding reproducibility of a substrate-structured device with the controllable preparation process of the device. Interestingly, the obvious promotion of J_{SC} for the Al-doped devices may be ascribed to the enhanced effectiveness of carrier collection and extraction and suppressed carrier recombination loss at the interface of Sb_2Se_3/CdS:Al.[22] A cross-sectional SEM image of the A3 device and the schematic structure is provided in the inset of **Figure 1(a)**. The Sb_2Se_3 absorber layer, CdS:Al

buffer layer, and ITO window layer were approximately 1200, 70, and 400 nm thick, respectively. The Sb_2Se_3 thin film consisted of large and compact crystal grains, confirming an effective combination reaction involved with sputtering and selenization of Sb precursor under sufficient Se vapor.[23] In addition, the heterojunction between the Sb_2Se_3 absorber layer and CdS:Al buffer layer presented good adhesion and a compact and benign pinhole-free interface without abrupt interfacial boundary. This high-quality heterojunction interface considerably reduces charge carrier recombination and current leakage, facilitating the collection of photogenerated carriers and echoing the enhancement of J_{SC}. [23, 24]

External quantum efficiency (EQE) characterization was applied to further explore photocurrent generation, as shown in **Figure 1(b)**. All devices clearly displayed broad photo-response ranging from ultraviolet to near-infrared region and possessed excellent quantum response, showing maximum EQE values of 90%, which are consistent with the strong light absorption of the intrinsically narrow bandgap of Sb_2Se_3 thin films.[25, 26] Importantly, the A3 device with appropriate Al cation incorporation exhibited considerable improvement in photocurrent generation at the visible region of 400–600 nm, compared with a non-doped counterpart. This variation indicated less light absorption loss by the buffer layer, along with the reduced carrier recombination loss at the Sb_2Se_3/CdS:Al heterojunction interface.[27] The optimization of device performance can be attributed to the proper concentration of Al cation doping in the CdS buffer layer, which not only alleviated the recombination loss of photo-generated carriers but also improved the carrier transport efficiency. The integrated J_{SC} values were calculated from EQE data according to the following equation:[28]

$$J_{SC} = \int F(\lambda) EQE(\lambda) d\lambda \quad (1)$$

where F(λ) is the photon flux and EQE(λ) is the measured EQE density. The integrated J_{SC} values for A1, A3, and A0 devices were 21.61, 25.33, and 21.10 mA/cm^2, respectively. Since part of the incident light might be blocked by the electrode probe during EQE measurement, the integrated J_{SC} is slightly lower, however, the J_{SC} variation agreed well with the *J–V* measurement results upon Al cation doping. The estimated bandgap (E_g) values obtained from the EQE spectra were 2.49 and 2.41 eV

for the A3 and A0 devices, respectively **(Figure 1 (c))**, revealing slight enlargement after Al cation doping.

To further investigate the correlation between the variation of E_g and the effect of the Al doping behavior, XPS characterizations were used in the representative Al-doped (A3) and A0 CdS thin films, along with a qualitative analysis of constituent elements and valence states. The spectra of the measured thin films were calibrated according to the peak of standard C 1s (284.68 eV).[29] The high-resolution XPS spectra of Cd, S, and Al elements fitted by the Gaussian method are displayed in **Figure 1 (d) and (f)**. According to Cd and S XPS spectra, no obvious differences can be identified in elemental chemical states between the two thin films, indicating the absence of phase transition or surface oxidation after doping. As shown in **Figure 1 (d)**, the Cd 3d peaks presented two characteristic peaks corresponding to $3d_{5/2}$ and $3d_{3/2}$, located at 404.9 and 411.7 eV, respectively.[30] In **Figure 1 (e)**, the position of the peaks centered at 161.4 and 162.5 eV of the S 2p spectrum were fitted by two main peaks ($2p_{3/2}$ and $2p_{1/2}$), which were associated to the only S^{2-} ion states belonging to CdS. The major peaks of Cd and S elements were assigned to high-resolution spectral deconvolution elemental states of CdS. Meanwhile, an observable peak of the Al 2p core levels for the A3 thin film in **Figure 1 (f)** was obtained at binding energy of 74.5 eV, indicating that the Al ion was successfully incorporated into the CdS film.[31]

Herein, given that device performance is closely associated with band alignment, the band structures of the A3 and A0 CdS samples were investigated using UPS measurements. As depicted in **Figure S6 (a) and (c)**, the cutoff edge (E_{cutoff}) values of binding energy near the surfaces of the A3 and A0 samples were 16.96 and 16.30 eV, respectively. Additionally, by extrapolating the linear region of low binding energy, the energy gaps (E_{onset}) between valence band maximum and Fermi energy were 2.02 and 1.98 eV, respectively. Thus, the conduction band (E_C), valence band (E_V), and Fermi levels (E_F) were calculated from the E_{cutoff} and E_{onset} values according to the following equation:[32]

$$\varphi = h\upsilon - E_{\mathrm{cutoff}} \quad (2)$$

$$E_{\mathrm{v}} = E_{\mathrm{cutoff}} + E_{\mathrm{onset}} \quad (3)$$

$$E_c = E_v - E_g \quad (4)$$

where φ is the work function, $h\upsilon$ is the ultraviolet photoelectron energy of 21.2 eV, and E_g is the band gap of the two samples calculated from EQE spectrum. The schematic diagrams of the band alignment for the pristine CdS device and Al-doped CdS device are depicted in **Figure 1 (g) and (h)**. Particularly, the energy level information of Sb_2Se_3 was obtained from the literature.[33] The CBO values of Sb_2Se_3/CdS and Sb_2Se_3/CdS:Al heterojunction were −0.21 and 0.19 eV, respectively. In the former device, a negative CBO (often referred to as "cliff-like") of −0.21 eV was found between the Sb_2Se_3/CdS interface, as clarified in **Figure 1 (g)**. This "cliff-like" band alignment intrinsically attenuated band bending because the low point of the conduction band in the CdS buffer layer in this case was located farther from the quasi-Fermi level of electrons.[34] More importantly, weak band bending would lower the barriers for charge carriers approaching the interface. As a result, electrons and holes near the Sb_2Se_3/CdS interface accumulated after they were separated by the electric field, and thus the probability of charge recombination via deep interfacial defects increased. By contrast, a positive CBO (often referred to as "spike-like") of 0.19 eV was observed after the device was treated with Al doping in the CdS buffer layer (**Figure 1 (h)**). Contrary to "cliff-like" band alignment, this "spike-like" band alignment prevented charge carriers from piling up in the vicinity of the heterojunction interface by increasing barriers that prevented charge carriers from reaching the interface.[26] Interface recombination can therefore be effectively restrained, giving rise to considerable promotion of carrier collection and ultimately the enhancement of J_{SC}. However, an extremely large "spike-like" CBO would inversely block photogenerated electrons reaching the CdS buffer side and diminish the device *J*sc and PCE. The CBO of our device (0.19 eV) was within the suitable range (0 < CBO < 0.4 eV) according to the values for the most efficient thin-film solar cells.[35] This optimal CBO between the heterojunction would efficiently suppress non-radiative recombination in the Sb_2Se_3/CdS:Al interface without affecting charge collection efficiency. Thus, we can preliminarily deduce that doping Al into the CdS buffer layer leads to the reasonable optimization of energy band alignment.

TEM measurement was performed on the champion Sb_2Se_3 device for the investigation of the Sb_2Se_3/CdS:Al heterojunction interface. The distinct cross-section TEM morphology of Sb_2Se_3/CdS:Al interface is shown in **Figure 2 (a1)**. A highly compact and void-free structure was observed, demonstrating a well-adherent Sb_2Se_3/CdS:Al heterojunction interface. HRTEM was subsequently conducted at the Al ion doping interface, which revealed benign lattice-matching characteristics (**Figure 2 (a2)**) corresponding to the compact and smooth feature in **Figure 2 (a1)**. Such an interface alleviates the current leakage and impedes the interfacial carrier recombination.[36] According to the atomic resolution HAADF-STEM images **(Figure 2 (b1))** obtained near the region of the Sb_2Se_3/CdS:Al interface (the yellow rectangle in **Figure 2 (a2))**, the measured lattice fringe with 0.329 nm matched well with the (111) plane of hexagonal CdS. **Figure 2 (b2)** displays the HAADF-STEM images of the bulk absorber layer (corresponding to the rose-red rectangle obtained from **Figure 2 (a2))**. A Sb_2Se_3 crystal with 1D crystal structure consisted of units $[Sb_4Se_6]_n$ ribbons formed by van der Waals forces and combined in the (001) direction by covalent Sb–Se bonds, which is conducive to carrier transport.[5] **Figure 2 (c1)** exhibits the intensity line profiles of a row of atoms corresponding to the yellow rectangle marked in **Figure 2 (b1)**. Notably, the atomic scale showed evident variation in column intensity, finding expression in an abnormal peak with lower intensity. It is likely to imply that the original site Cd atoms were substituted by another cation that possesses a relatively smaller atomic number, that is, Al atoms from doping engineering. Finally, the elemental composition distribution of the cross-section of the device was characterized through scanning transmission electron microscopy combined with energy dispersive X-ray spectroscopy mapping **(Figure 2 (d))**. Each corresponding element in the absorber and buffer layers showed a uniform distribution, implying the successful doping of Al cation. Overall, Al doping into CdS can improve the heterojunction, observed as a benign microstructural Sb_2Se_3/CdS:Al interface, which enhanced device performance and was accompanied by a high-quality Sb_2Se_3 absorber layer.

To examine the surface electrical properties of pristine CdS (A0) and Al-doped CdS (A3) samples, we carried out Kelvin probe force microscopy (KPFM) measurements.

AFM micrograph (**Figure 3 (a) and (e)**) and the contact potential differences (V_{CPD}, the difference between the probe and sample; **Figure 3 (b) and (f)**) of the two samples are shown in **Figure 3**. By taking line profiles along the marked area, the potential mappings compared with topography were obtained (**Figure 3 (c) and (g)**). As can be observed in the two samples, GBs possessed a high V_{CPD} compared with the grain surface (GS), corresponding to a low work function, meaning the E_F of GBs was closer to the vacuum level, which were schematically depicted in **Figure 3 (d) and (h)**. This increase in V_{CPD} at the GBs impeded carrier transport across the horizontal direction. By contrast, the low V_{CPD} at GS was ascribed to the relatively small lateral potential difference thus photo-generated electrons and holes were effectively separated along the aligned $[Sb_4Se_6]_n$ ribbons.[37] In the comparison of the surface potentials of the two thin films, the contact potential differences for samples with incorporated Al cation (~15 mV) were smaller than that for the pristine CdS samples (~60 mV). This result indicated less energy variation at the Fermi level and reduced band fluctuation in the Al-doped CdS device.[38] Consequently, the variety of V_{CPD} in Al-doped CdS device is beneficial for charge carrier extraction and collection, facilitating carrier transport across the $[Sb_4Se_6]_n$ ribbons and improving device performance.

Dark *J*–*V* measurements were conducted under a bias voltage of −1 to 1 V, and the electrical properties of the representative devices were estimated. The three devices (A0, A1, and A3) showed evident rectifying characteristics, as indicated by the *J*–*V* curves in **Figure S7**. Subsequently, shunt conductance (*G*), series resistance (*R*), diode ideality factor (*A*), and reverse saturation current density (J_0), were compared according to the dark *J*–*V* curves and the following single exponential diode formula with Site's method:[39]

$$J = J_0 exp\left[\frac{q}{AkT}(V - JR)\right] + GV - J_L \quad (5)$$

The *G* values were 3.18, 2.46, and 3.72 mS/cm for A1, A3, and A0, respectively, through extracting the flat district of the plot of *dJ/dV* versus *V* with the reverse bias condition **(Figure 4 (a))**. The values of *R* and *A* were derived from the curves of *dV/dJ* versus $(J+J_{SC})^{-1}$, as shown in **Figure 4 (b)**, via calculating the intercept of the Y-axis

and the slope as AkT/q, respectively. The R value was 2.07 Ω cm^2 (R_{A3}) in the A3 device while then increased to 3.69 Ω cm^2 (R_{A0}) in the A0 device. The A values were 2.05, 1.84, and 2.07 for A1, A3, and A0 devices, respectively. By plotting the semi-logarithmic ln(J+J_{SC}-GV) versus V-RJ **(Figure 4 (b))**, the J_0 values for the A3 and A0 devices were 6.6 × 10^{-4} and 1.1× 10^{-3} mA/cm^2, respectively. In fact, the results of A and J_0 were utilized as effective standards that reflect the carrier recombination circumstance of defects at the interface and bulk.[40] Notably, the low A value implied that doping Al into CdS suppressed carrier recombination losses in the devices. Moreover, the smaller J_0 indicated effective carrier transportation and further inhibited shunting paths.[41] Enhanced charge transport and reduced carrier recombination were indicated by significant enhancement in shut resistance (R_{SH}) [42] exhibited in **Table S1**. Hence, under an appropriate Al doping concentration in CdS, considerably improved Sb_2Se_3/CdS:Al junction quality was achieved, as evidenced by the preferable A, small J_0, and increased R_{SH}, leading to the greatly enhanced J_{SC} for the A3 sample.[22]

Defects often act as recombination centers deteriorating device performance. It is extremely significant that the defect states and the qualitative defect density of the device should be thoroughly investigated with the space charge limited current (SCLC) mode.[43] The J–V logarithmic curves for the A1, A3, and A0 devices under dark conditions are displayed in **Figure 4 (d-f)**, respectively. In general, the curves can be classified according to their exponent n values: the ohmic region of low voltage (n = 1, yellow rectangle),[44] trap-filled limit (TFL) region of middle voltage (n > 3, red rectangle), and child region of high voltage (n = 2, green rectangle). The TFL voltage (V_{TFL}) was defined as the cross point of the TFL and ohmic regions. The current density abruptly increased when the bias voltage exceeded the V_{TFL}, representing the trap states are entirely filled by the injected carriers in the TFL region.[45] Thus, the obtained values were 0.22, 0.19, and 0.25 V for the A1, A3, and A0 devices, respectively. The defect density N_{trap} of the device can be determined as follows:[26]

$$N_{\text{trap}} = \frac{2\varepsilon\varepsilon_0 V_{\text{TFL}}}{eL^2} \quad (6)$$

where ε represents the vacuum dielectric constant, ε_0 represents the relative dielectric

constant of Sb_2Se_3 (generally selected as 15.1),[26] L is the thickness of Sb_2Se_3 thin films, and e is the elementary charge. According to the formula, N_{trap} decreased with V_{TFL}. The obtained N_{trap} values for Al-doped CdS devices were smaller than that for the A0 devices, calculated as 2.55×10^{14}, 2.20×10^{14}, and 2.90×10^{14} cm^{-3} for the A1, A3, and A0 devices, respectively. Fewer defect recombination centers at the grain boundary and Sb_2Se_3/CdS:Al interface led to the high-quality Sb_2Se_3 absorber layer and the CdS buffer layer doped with Al cation.[46]

It is meaningful to investigate the behavior of interface defect recombination, which always plays a crucial role in unveiling device performance improvement mechanisms. Herein, capacitance–voltage (C–V) profiling and deep-level capacitance profiling (DLCP) characterizations regarding as a vital electrical property characterization technique, were further carried out to estimate the concentration and properties of interfacial defects for our solar cells. Generally, C–V characterization, driven by DC voltage, represents the response of interface defects, bulk defects, and free carriers. DLCP characterization, driven by a small AC voltage under different bias voltages at 100 kHz, reflects the response of bulk defects and free carriers.[47] Thus, the discrepancy at zero bias between the C–V-measured defect density (N_{CV}) and the DLCP-measured defect density (N_{DLCP}) is connected to the interfacial defect density (N_i) of Sb_2Se_3 devices. The C–V and DLCP characterizations as a function of the depletion region width (W_d) are displayed in **Figure 5 (a)**, according to the following expressions:[12]

$$N_{CV} = \frac{-2\varepsilon_{r,n}N_D}{\left(\frac{d\left(1/C^2\right)}{dV}\right)qA^2\varepsilon_0\varepsilon_{r,n}N_D + 2\varepsilon_{r,p}} \quad (7)$$

$$N_{DLCP} = -\frac{C_0^3}{2q\varepsilon_0\varepsilon_{r,p}A^2C_1} \quad (8)$$

$$W_d = \frac{\varepsilon_0\varepsilon_{r,p}A}{C_0} \quad (9)$$

where A symbolizes the device area, ε_0 represents the vacuum permittivity, $\varepsilon_{r,n}$ and N_D are the relative permittivity and the doping density of CdS, respectively. $\varepsilon_{r,p}$ is the relative permittivity of Sb_2Se_3, C_0 and C_1 are two quadratic fitting parameters originated from the C–V curves. The detailed analysis data of C–V and DLCP profiling are shown in **Table 2**. The interfacial defect density decreased after Al doping of CdS. Specifically,

the calculated N_i values for the A0 device was 4.90×10^{16} cm^{-3}, and the corresponding values for the A1 and A3 devices decreased to 3.08×10^{16} and 3.93×10^{16} cm^{-3}, respectively, demonstrating low defect density and reduced recombination loss at the optimal Sb_2Se_3/CdS:Al interface. In addition, the Al-doped A3 device possessed a large W_d of 193 nm, which is conducive to carrier extraction and light absorption in the device [23] and obviously enhances the J_{SC} values and performance of the Al-doped devices. Deep-level transient spectroscopy (DLTS) is vital to obtaining insights into bulk defect properties, including defect concentration, type, and defect energy level of a photovoltaic device. [48, 49] The DLTS results of the A0 and A3 device are exhibited in **Figure 5 (b)**, containing positive peaks and negative DLTS signal peaks. The positive peaks in the DLTS curves can be ascribed to majority carrier traps, whereas negative peaks represent minority carrier traps. Herein, positive and negative curves corresponded to electron and hole traps in the Sb_2Se_3 absorber,[48] respectively. The defect information of the two categories of devices is calculated and summarized in **Table 3**, including the value of defect active energy (E_r), defect density (N_T), and capture cross-section (σ). Especially, the E_r (E_C–E_T or E_T–E_V, wherein, E_T, E_C, and E_V are the defect energy level, conduction band edge, and valance band edge, respectively) of the defects were obtained through the linear fitting of DLTS signal derived Arrhenius plot points (**Figure 5 (c)**), using the following equations: [48, 50]

$$\ln\left(\tau_e \upsilon_{th,n} N_C\right) = \frac{E_C - E_T}{k_B T} - \ln(X_n \sigma_n) \quad (10)$$

$$\ln\left(\tau_e \upsilon_{th,p} N_V\right) = \frac{E_T - E_V}{k_B T} - \ln(X_p \sigma_p) \quad (11)$$

where τ_e is the emission time constant, $\upsilon_{th,n}$ and $\upsilon_{th,p}$ are the thermal velocity, N_C, N_V represent conduction band state density and valence band state density, respectively. X_n and X_p are the entropy factor for electron and hole. One positive and one negative peak were found in both devices, demonstrating one hole trap defect and one electron trap, which were denoted as H1 and E1, respectively**.** The corresponding energy level of the negative peak for the A3 device was detected at 0.225 eV, with an N_T and σ of 2.28×10^{14} cm^{-3} and 1.98×10^{-20} cm^2, respectively. The A0 device exhibited a similar defect type E1 located at about 0.251 eV, which was close to the intrinsic Fermi level (E_F),

along with an adversely increased N_T of 3.73 × 10^{14} cm^{-3} and the largest σ of 6.56 × 10^{-20} cm^2. According to the calculated results of energy level, the defect type E1 can be assigned as Se vacancy (V_{Se}) defect, agreeing well with our previous works that the Sb_2Se_3 thin films were fabricated by sputtering and selenization technique.[3, 26, 33]In addition, in the positive peaks, a defect type denoted as H1 (E_r = 0.303 eV, N_T = 2.50 × 10^{14} cm^{-3}, and σ = 5.88×10^{-21} cm^2) was obtained for the A3 device, whereas the A0 device displayed a similar hole trap H1 (E_r = 0.377 eV, N_T = 4.57 × 10^{14} cm^{-3}, and σ = 4.55 × 10^{-20} cm^2), which can be assigned selenium antisite (Se_{Sb}) according to the DFT calculations.[51] Notably, the decreased defect density and capture cross-section of the Sb_2Se_3 device with the doping of Al cation in CdS improved performance. Furthermore, the index N_T×σ is another effective pathway to investigate the defect feature for thin-film solar cells, according to the following equation:[9]

$$\tau_{\mathrm{trap}} = \frac{1}{v_t \sigma N_T} \tag{12}$$

where σ and N_T are the capture cross-section and defect density acquired from DLTS results, v_t is the carrier thermal velocity, which is approximately 10^7 cm s^{-1} at room temperature in the bulk of semiconductors.[52] As listed in **Table 3** and the histogram displayed in **Figure 5(d)**, the obviously decreased value N_T×σ demonstrated the effective passivation of the two major defects (E1 and H1) in our devices owing to the Al cation doped into the CdS buffer layer and the post-annealing treatment. The photogenerated electrons and holes are likely to be captured and result in poor trap-assisted recombination, ultimately reducing the minority carrier lifetime and decreasing J_{SC}.[53] After the doping of Al cation into the CdS buffer layer, the capture cross-section of H1 dramatically decreased by nearly one order of magnitude. The carriers captured by shallow trap states are emitted again in an extremely short time because of the small capture cross-section.

The energy states and defect levels of the two devices are revealed in **Figure 5 (e) and (f)**, respectively. In the A0 device, the corresponding defect level E1 extracted from the Arrhenius plots was located at 0.251 eV below E_C, and the H1 defect was located at 0.377 eV above E_V, which were closer to the position of intrinsic E_F. These conditions

can lead to severe defect-assisted recombination because of the detrimental pining effect. By contrast, in the A3 device, the defect levels E1 and H1 were detected at 0.225 eV below E_C and 0.303 eV above E_V and effectively passivated the harmful defects, thereby alleviating the pining effect, facilitating the split of the quasi-Fermi levels of holes and electrons, and enhancing J_{SC}.

To elucidate the behavior of defect recombination and carriers' transport dynamic mechanism, electrochemical impedance spectroscopy (EIS) measurements were carried out for the A0 and A3 devices. The corresponding Nyquist plots of the EIS spectrum and equivalent circuit diagrams of the devices are represented in **Figure S8**. The impedance spectra were fitted by the equivalent circuit, which was composed of two modules. The first part belongs to the Sb_2Se_3/CdS:Al heterojunction interface, and the second part represents the remaining devices. The series resistance (R_S) obtained by the intercept of the X-axis represents the contact and material resistance of the whole cell, and the recombination resistance (R_{rec}) is equal to the diameter of the impedance spectrum semicircle and represents the defect recombination resistance of the heterojunction interface.[41] Notably, the R_S values of the A3 device (21.33 Ω) was smaller than that of the A0 device (23.52 Ω) because of carrier transfer enhanced by the incorporation of Al cation. The value of R_{rec} for the A0 and A3 devices were 13637 and 2826 Ω, respectively, which implied efficient defect passivation at the Sb_2Se_3/CdS:Al interface. The enhanced carrier generation, separation, and transport and the suppressed recombination led to the overall enhancement of Al-doped device performance.

3. Conclusion

We have demonstrated an effective strategy of Al^{3+} cation doping in the CdS buffer layer through spin-coating and post-annealing methods. The Sb_2Se_3 devices with substrate configuration of Mo/Sb_2Se_3/CdS:Al/ITO/Ag were constructed, and the key device performance was systematically investigated. Al doping on CdS significantly optimized the band alignment and the heterojunction interface quality, leading to the facilitation of charge carrier transport and the suppression of interface recombination. Meanwhile, post-annealing treatment was beneficial to passivate bulk defects and

defect-assisted recombination. Finally, after the introduction of 0.5 mol Al^{3+} ion to the CdS buffer layer and annealing at 280 °C for 5 min, the thin-film device achieved a high PCE of 8.41% and showed dramatic increase in *J*sc (from 22.98 mA/cm^2 to 28.26 mA/cm^2). This work provides an effective and facile method for fabricating highly efficient Sb_2Se_3 thin-film solar cells, broadening the development of chalcogenide-based photovoltaic devices.

4. Experimental Section

Deposition of Sb_2Se_3 thin film: Mo-coated glass as back contact layer was employed for the Sb_2Se_3 solar cell fabrication. An RF magnetron sputtering Sb metallic precursor thin film was sequentially deposited on the Mo-coated glass which was entirely cleaned in an ultrasonic bath using detergent, ethanol, and deionized water. Before the magnetron sputtering process, the back pressure of the vacuum chamber was kept below 7.0×10^{-4} Pa. The optimized sputtering power and pressure were evacuated at 35 W and 0.5 Pa in order to reach high-quality Sb thin film with fewer voids and benign adhesion. The flow rate of argon is 30 sccm, and the sputtering process was conducted for 40 min. Sequentially, an effective post-selenization heat treatment was induced to the in-situ combination reaction and self-assembled growth of Sb_2Se_3 thin films with high-crystallinity. The details are described in our previous publication.[19]

Preparation of Al-doped CdS buffer layer: After finishing the preparation of Sb_2Se_3 absorber layer, the pristine cadmium sulfide (CdS) buffer layer was then deposited onto the well-crystalline Sb_2Se_3 thin film employing chemical bath deposition (CBD) technique. The aqueous solution of $CdSO_4$ (0.015 M), thiourea (0.75 M), and ammonium hydroxide (≥28%) were subsequently added to deionized water. The samples were fully soaked into the well-mixed solution which was then placed in a preheated 80 ℃ water bath with continuous stirring for 9 min. After completing the chemical reaction, the samples were rinsed with deionized water and dried in an oven. For Al doping, a series amount of $AlCl_3$ (99.999%, Aladdin) powder was weighed and absolutely dissolved in an organic solvent of 2-methoxy ethanol to prepare Al^{3+} solution with variable concentration, i.e., 0.1 M, 0.3 M, 0.5 M and 0.7 M. A schematic

illustration of Al-doped CdS film deposition via spin coating and post-annealing process is depicted at the center of **Figure S1**. Different concentration Al^{3+} solution was spin-coated on the surface of Sb_2Se_3/CdS film and then conducted a heat treatment on a hot plate at various temperatures (i.e., 260 °C, 280 °C, 300 °C, and 320 °C) and different durations (i.e., 1 min, 3 min, 5 min, and 7 min). The thickness of Al-doped CdS buffer layer was approximately 70 nm.

Fabrication of Mo/Sb_2Se_3/CdS:Al/ITO/Ag solar cells: Indium tin oxide (ITO), used as a windows layer, was subsequently covered on the surface of Al-doped CdS film via direct current (DC) magnetron sputtering method. The sputtering procedure was performed with a power of 120 W, and a relatively low deposition pressure of 0.4 Pa. Pure argon gas and oxygen gas were introduced at a flow rate of 40 and 30 sccm, respectively. The surface of the device was divided into small squares with an identical active area of 0.075 cm^2. Ag electrodes were thermally evaporated onto the ITO surface to form metallic contact. Overall, Figure S1 shows a schematic diagram of the fabrication process of this thin-film solar cell with the configuration of Glass/Mo/Sb_2Se_3/CdS: Al/ITO/Ag **(Figure S1)**.

Characterizations: The crystal structure of Sb_2Se_3 thin film was conducted by X-ray diffraction (XRD, Ultima-iv) with *Cu Kα* radiation under the test environment of 40 kV and 40 mA. The morphology of Sb_2Se_3 thin film and cross-sectional images of the devices were characterized by scanning electron microscope (SEM, SUPRA 55). Current density–voltage (*J*−*V*) characteristics of the Sb_2Se_3 thin film devices were represented by a Keithley 2400 multi-meter under standard test conditions (100 mW/cm^2, AM1.5 G, 25 °C). Prior to *J*−*V* measurements, test system was calibrated with Si reference cell. The external quantum efficiency (EQE) spectrum was carried out using a Zolix SCS101 system and a Keithley 2400 source meter. X-ray photoelectron spectroscopy (XPS ESCALAB 250Xi) measurement was performed to analyze the doping nature and valence states of Al-doped CdS thin films. The band level information of the CdS/Sb_2Se_3 interface was determined through ultraviolet photoelectron spectroscopy (UPS, Thermo Fisher spectrometer). Transmission electron microscope (TEM) was conducted to characterize the microstructural and

morphological using a FEI Titan Cubed Themis G2 300 microscope. Energy dispersive spectroscope (EDS) coupled with TEM were used to analyze the elemental distribution. The topographies and surface potential of the thin films were analyzed by Kelvin Electrostatic Force Microscopy (KPFM, Dimension Icon, Bruker), which is a non-contact AFM technique applied to investigate the surface potential distribution. Capacitance-voltage ($C-V$) profiling were employed at a frequency of 10 kHz, an alternating-current (AC) amplitude of 30 mV, and the bias voltage from −0.5 to 0.1 V at the dark condition. An AC amplitude from 20 to 140 mV and a direct-current (DC) bias voltage from −0.25 to 0.1 V were applied to measure drive-level capacitance profiling (DLCP). The deep-level transient spectroscopy (DLTS) result was obtained through an FT-1030 HERA DLTS system configured with a JANIS VPF-800 cryostat controller. The electrochemical impedance spectra (EIS) were conducted by Zennium electrochemical workstation under dark condition.

Supporting Information

Supporting Information is available from the Wiley Online Library or from the author.

Acknowledgments

Y. Luo and G. Chen contributed equally. This work was supported by National Natural Science Foundation of China (No. 62074102, 62104156), Guangdong Basic and Applied Basic Research Foundation (2022A1515010979) China, Key Project of Department of Education of Guangdong Province (No. 2018KZDXM059) China, Science and Technology plan project of Shenzhen (20220808165025003, 20200812000347001 and JCYJ20190808153409238) China. The authors wish to acknowledge the assistance on HAADF-STEM observation received from the Electron Microscope Center of the Shenzhen University.

Conflict of interest

The authors declare no conflict of interest.

Data Availability Statement

The data that support the findings of this study are available from the corresponding author upon reasonable request.

Received: ((will be filled in by the editorial staff))
Revised: ((will be filled in by the editorial staff))
Published online: ((will be filled in by the editorial staff))

References

[1] H. Li, L. M. Lin, L. Q. Yao, F. Y. Wu, D. Wei, G. L. Liu, Z. G. Huang, S. Y. Chen, J. M. Li, G. L. Chen, *Adv. Funct. Mater.* **2022,** *32*, 2110335.

[2] S. Y. Wang, Y. Q. Zhao, L. Q. Yao, C. Li, J. B. Gong, G. L. Chen, J. M. Li, X. D. Xiao, *Sci. Bull.* **2022,** *67*, 263.

[3] R. Tang, S. Chen, Z. H. Zheng, Z. H. Su, J. T. Luo, P. Fan, X. H. Zhang, J. Tang, G. X. Liang, *Adv. Mater.* **2022,** *34*, 2109078.

[4] W. T. Lian, R. Cao, G. Li, H. L. Cai, Z. Y. Cai, R. F. Tang, C. F. Zhu, S. F. Yang, T. Chen, *Adv. Sci.* **2022,** *9*, 2105268.

[5] Z. T. Duan, X. Y. Liang, Y. Feng, H. Y. Ma, B. L. Liang, Y. Wang, S. P. Luo, S. F. Wang, R. E. I. Schropp, Y. H. Mai, Z. Q. Li, *Adv. Mater.* **2022,** *34*, 2202969.

[6] W. J. Tao, L. L. Zhu, K. H. Li, C. Chen, Y. Z. Chen, Y. J. Li, X. F. Li, J. Tang, H. H. Shang, H. M. Zhu, *Adv. Sci.* **2022,** *9*, 2202154.

[7] H. L. Cai, R. Cao, J. X. Gao, C. Qian, B. Che, R. F. Tang, C. F. Zhu, T. Chen, *Adv. Funct. Mater.* **2022,** *9*, 2208243.

[8] Z. Q. Li, X. Y. Liang, G. Li, H. X. Liu, H. Y. Zhang, J. X. Guo, J. W. Chen, K. Shen, X. Y. San, W. Yu, R. E. I. Schropp, Y. H. Mai, *Nat. Commun.* **2019,** *10*, 125.

[9] Y. Q. Zhao, S. Y. Wang, C. Li, B. Che, X. L. Chen, H. Y. Chen, R. F. Tang, X. M. Wang, G. L. Chen, T. Wang, J. B. Gong, T. Chen, X. D. Xiao, J. M. Li, *Energy Environ. Sci.* **2022**, https://doi.org/10.1039/D2EE02261C.

[10] W. Han, D. Gao, R. Tang, Y. Ma, C. Jiang, G. Li, T. Chen, C. Zhu, *Solar RRL* **2021,** *5*, 202000750.

[11] Q. Q. Gao, S. J. Yuan, Z. J. Zhou, D. X. Kou, W. H. Zhou, Y. N. Meng, Y. F. Qi, L. T. Han, S. X. Wu, *Small* **2022,** *18*, 2203443.

[12] G. X. Liang, Y. D. Luo, S. Chen, R. Tang, Z. H. Zheng, X. J. Li, X. S. Liu, Y. K.

Liu, Y. F. Li, X. Y. Chen, Z. H. Su, X. H. Zhang, H. L. Ma, P. Fan, *Nano Energy* **2020,** *73*, 104806.

[13] G. X. Liang, Y. D. Luo, S. Chen, R. Tang, Z. H. Zheng, X. J. Li, X. S. Liu, Y. K. Liu, Y. F. Li, X. Y. Chen, Z. H. Su, X. H. Zhang, H. L. Ma, P. Fan, Nano Energy 2020, 73, 104806.

[14] X. X. Wen, C. Chen, S. C. Lu, K. H. Li, R. Kondrotas, Y. Zhao, W. H. Chen, L. Gao, C. Wang, J. Zhang, G. D. Niu, J. Tang, *Nat. Commun.* **2018,** *9*, 2179.

[15] Y. J. Chen, Y. Y. Wang, R. Wang, X. B. Hu, J. H. Tao, G. E. Weng, C. H. Zhao, S. Q. Chen, Z. Q. Zhu, J. H. Chu, H. Akiyama, *ACS Appl. Energy Mater.* **2020,** *3*, 10415.

[16] C. Z. Ou, K. Shen, Z. Q. Li, H. B. Zhu, T. L. Huang, Y. H. Mai, *Sol. Energy Mater. Sol. Cells* **2019,** *194*, 47.

[17] H. Ning, H. F. Guo, J. Y. Zhang, X. Wang, X. G. Jia, J. H. Qiu, N. Y. Yuan, J. N. Ding, *Sol. Energy Mater. Sol. Cells* **2021,** *221*, 110816.

[18] C. Chen, X. X. Liu, K. H. Li, S. C. Lu, S. Y. Wang, S. Li, Y. Lu, J. G. He, J. J. Zheng, X. T. Lin, J. Tang, *Appl. Phys. Lett.* **2021,** *118*, 172103.

[19] C. Y. Wu, C. H. Jiang, X. M. Wang, H. H. Ding, H. X. Ju, L. J. Zhang, T. Chen, C. F. Zhu, *ACS Appl. Mater. Interfaces* **2019,** *11*, 3207.

[20] K. H. Li, C. Chen, S. C. Lu, C. Wang, S. Y. Wang, Y. Lu, J. Tang, *Adv. Mater.* **2019,** *31*, 44.

[21] S. Rijal, D. B. Li, R. A. Awni, C. X. Xiao, S. S. Bista, M. K. Jamarkattel, M. J. Heben, C. S. Jiang, M. Al-Jassim, Z. N. Song, Y. F. Yan, *Adv. Funct. Mater.* **2022,** *32*, 2110032.

[22] W. H. Wang, Z. X. Cao, H. H. Wang, J. S. Luo, Y. Zhang, *J. Mater. Chem. A* **2021,** *9*, 26963.

[23] Y. D. Luo, R. Tang, S. Chen, J. G. Hu, Y. K. Liu, Y. F. Li, X. S. Liu, Z. H. Zheng, Z. H. Su, X. F. Ma, P. Fan, X. H. Zhang, H. L. Ma, Z. G. Chen, G. X. Liang, *Chem. Eng. J.* **2020,** *393*, 124599.

[24] Z. L. Yang, X. M. Wang, Y. Z. Chen, Z. F. Zheng, Z. Chen, W. Q. Xu, W. M. Liu, Y. Yang, J. Zhao, T. Chen, H. M. Zhu, *Nat. Commun.* **2019,** *10*, 4540.

[25] D. Liu, R. F. Tang, Y. Y. Ma, C. H. Jiang, W. T. Lian, G. Li, W. H. Han, C. F. Zhu, T. Chen, *ACS Appl. Mater. Interfaces* **2021,** *13*, 18856.

[26] G. X. Liang, M. D. Chen, M. Ishaq, X. R. Li, R. Tang, Z. H. Zheng, Z. H. Su, P.

Fan, X. H. Zhang, S. Chen, *Adv. Sci.* **2022,** *9*, 202105142.

[27] Z. H. Su, K. W. Sun, Z. L. Han, H. T. Cui, F. Y. Liu, Y. Q. Lai, J. Li, X. J. Hao, Y. X. Liu, M. A. Green, *J. Mater. Chem. A* **2014,** *2*, 500.

[28] Y. L. Pei, J. Guo, D. X. Kou, W. H. Zhou, Z. J. Zhou, Q. W. Tian, Y. N. Meng, S. X. Wu, *Sol. Energy* **2017,** *148*, 157.

[29] S. Chen, T. X. Liu, M. D. Chen, M. Ishaq, R. Tang, Z. H. Zheng, X. J. Li, X. S. Qiao, G. X. Liang, *Nano Energy* **2022,** *99*, 107417.

[30] M. Y. Leng, C. Chen, D. J. Xue, J. B. Gong, Y. H. Liu, K. H. Li, X. D. Xiao, G. Wang, J. Tang, *Sol. Energy Mater. Sol. Cells* **2021,** *225*, 111043.

[31] M. Jiang, Z. J. Wu, X. Y. Zhang, Y. Y. Cai, W. Z. Wang, Y. J. Liang, *Energy Convers. Manage.* **2022,** *268*, 115978.

[32] Y. D. Luo, M. D. Chen, R. Tang, M. Azam, S. Chen, Z. H. Zheng, Z. H. Su, P. Fan, H. L. Ma, G. X. Liang, X. H. Zhang, *Sol. Energy Mater. Sol. Cells* **2022,** *240*, 111721.

[33] R. Tang, Z. H. Zheng, Z. H. Su, X. J. Li, Y. D. Wei, X. H. Zhang, Y. Q. Fu, J. T. Luo, P. Fan, G. X. Liang, *Nano Energy* **2019,** *64*, 103929.

[34] C. Yan, J. L. Huang, K. W. Sun, S. Johnston, Y. F. Zhang, H. Sun, A. B. Pu, M. R. He, F. Y. Liu, K. Eder, L. M. Yang, J. M. Cairney, N. J. Ekins-Daukes, Z. Hameiri, J. A. Stride, S. Y. Chen, M. A. Green, X. J. Hao, *Nat. Energy* **2018,** *3*, 764.

[35] Y. Li, K. Wang, D. W. Huang, L. T. Li, J. H. Tao, N. A. A. Ghany, F. Jiang, *Appl. Catal., B* **2021,** *286*, 119872.

[36] G. X. Liang, T. X. Liu, M. Ishaq, Z. J. Chen, R. Tang, Z. H. Zheng, Z. H. Su, P. Fan, X. H. Zhang, S. Chen, *Chem. Eng. J.* **2022,** *431*, 133359.

[37] W. Yang, J. H. Kim, O. S. Hutter, L. J. Phillips, J. W. Tan, J. Park, H. Lee, J. D. Major, J. S. Lee, J. Moon, *Nat. Commun.* **2020,** *11*, 861.

[38] M. Vishwakarma, M. Kumar, M. Hendrickx, J. Hadermann, A. P. Singh, Y. Batra, B. R. Mehta, *Adv. Mater. Interfaces* **2021,** *8*, 2002124.

[39] C. Liu, S. H. Wu, Y. Y. Gao, Y. Feng, X. L. Wang, Y. F. Xie, J. Z. Zheng, H. B. Zhu, Z. Q. Li, R. E. I. Schropp, K. Shen, Y. H. Mai, *Adv. Funct. Mater.* **2022**, 2209601.

[40] K. Shen, Y. Zhang, X. Q. Wang, C. Z. Ou, F. Guo, H. B. Zhu, C. Liu, Y. Y. Gao, R. E. I. Schropp, Z. Q. Li, X. H. Liu, Y. H. Mai, *Adv. Sci.* **2020,** *7*, 2001013.

[41] W. H. Wang, Z. X. Cao, X. Zuo, L. Wu, J. S. Luo, Y. Zhang, *J. Energy Chem.* **2022,** *70*, 191.

[42] H. F. Guo, C. Zhao, Y. L. Xing, H. J. Tian, D. C. Yan, S. Zhang, X. G. Jia, J. H. Qiu, N. Y. Yuan, J. N. Ding, *J. Phys. Chem. Lett.* **2021,** *12*, 12352.

[43] K. Chen, P. Wu, W. Q. Yang, R. Su, D. Y. Luo, X. Y. Yang, Y. G. Tu, R. Zhu, Q. H. Gong, *Nano Energy* **2018,** *49*, 411.

[44] P. Fan, G. J. Chen, S. Chen, Z. H. Zheng, M. Azam, N. Ahmad, Z. H. Su, G. X. Liang, X. H. Zhang, Z. G. Chen, *ACS Appl. Mater. Interfaces* **2021,** *13*, 46671.

[45] G. Jang, H. C. Kwon, S. Ma, S. C. Yun, H. Yang, J. Moon, *Adv. Energy Mater.* **2019,** *9*, 1901719.

[46] C. Wang, S. C. Lu, S. Li, S. Y. Wang, X. T. Lin, J. Zhang, R. Kondrotas, K. H. Li, C. Chen, J. Tang, *Nano Energy* **2020,** *71*, 104577.

[47] X. X. Wen, Z. H. Lu, G. C. Wang, M. A. Washington, T. M. Lu, *Nano Energy* **2021,** *85*, 106019.

[48] W. T. Lian, C. H. Jiang, Y. W. Yin, R. F. Tang, G. Li, L. J. Zhang, B. Che, T. Chen, *Nat. Commun.* **2021,** *12*, 3260.

[49] D. V. Lang, *J. Appl. Phys.* **1974,** *45*, 3023.

[50] R. F. Tang, X. M. Wang, W. T. Lian, J. L. Huang, Q. Wei, M. L. Huang, Y. W. Yin, C. H. Jiang, S. F. Yang, G. C. Xing, S. Y. Chen, C. F. Zhu, X. J. Hao, M. A. Green, T. Chen, *Nat. Energy* **2020,** *5*, 587.

[51] C. Chen, J. Tang, ACS Energy Lett. 2020, 5, 2294.

[52] S. Y. Wang, Y. Q. Zhao, B. Che, C. Li, X. L. Chen, R. F. Tang, J. B. Gong, X. M. Wang, G. L. Chen, T. Chen, J. Li, X. D. Xiao, *Adv. Mater.* **2022**, https://doi.org/10.1002/adma.202206242.

[53] S. Hadke, M. L. Huang, C. Chen, Y. F. Tay, S. Y. Chen, J. Tang, L. Wong, *Chem. Rev.* **2022,** *122*, 10170.

Table 1. Effects of Al-doping concentration on the photovoltaic performance.

Devices	Concentration (mol)	PCE (%)	V_{OC} (mV)	FF (%)	J_{SC} (mA/cm^2)
A1	0.1	7.01	489	61.12	23.47
A2	0.3	7.49	475	62.75	25.14
A3	0.5	8.41	489	60.87	28.26
A4	0.7	7.24	484	61.92	24.15
A0	0	6.82	515	57.92	22.98

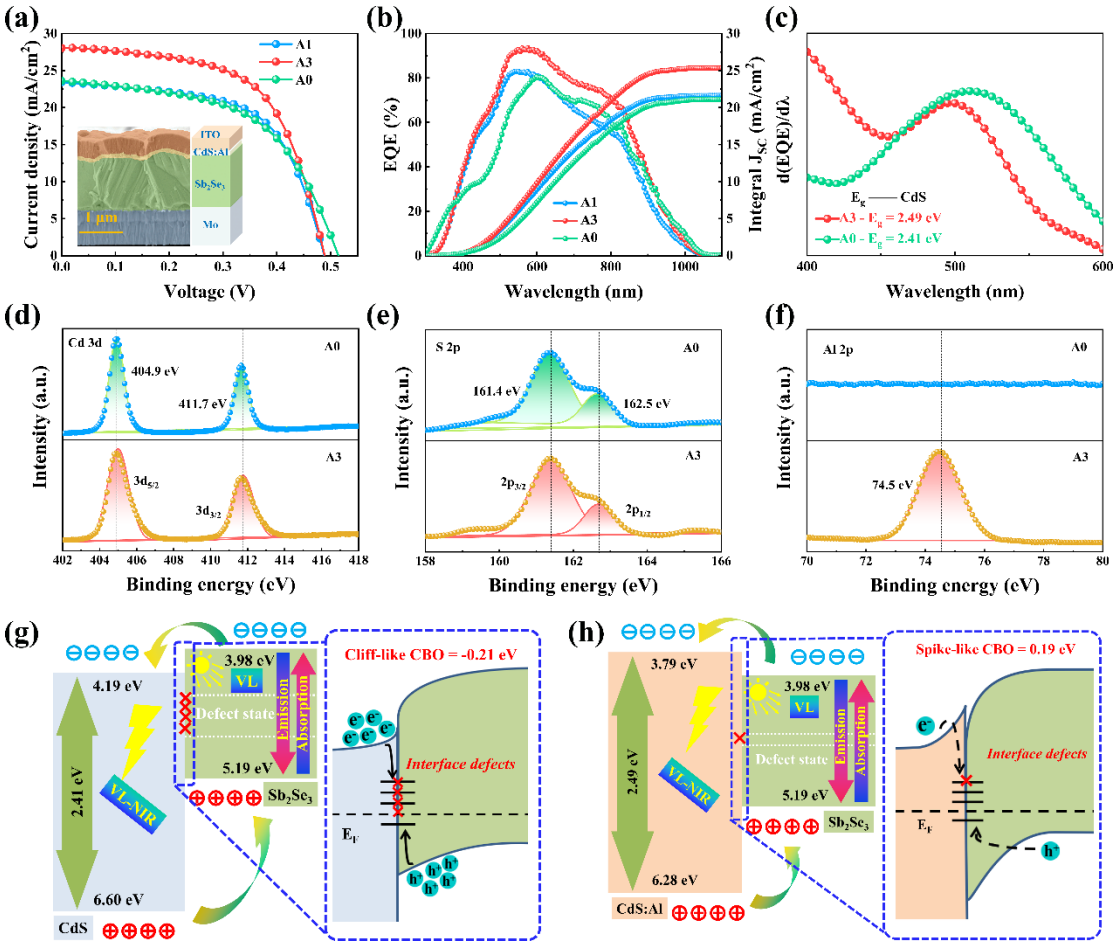

Figure 1. (a) Current density–voltage (*J–V*) curves, and (b) External quantum efficiency (EQE) together with integrated J_{SC} of the representative A1, A3 and A0 devices, respectively. (c) The E_g values obtained from EQE spectra. XPS analysis of Cd 3d (d), S 2p (e), and Al 2p (f) for the representative pristine CdS and Al-doped CdS thin films. Schematic illustration of the band alignment for pristine CdS (g) and Al-doped CdS (h) devices.

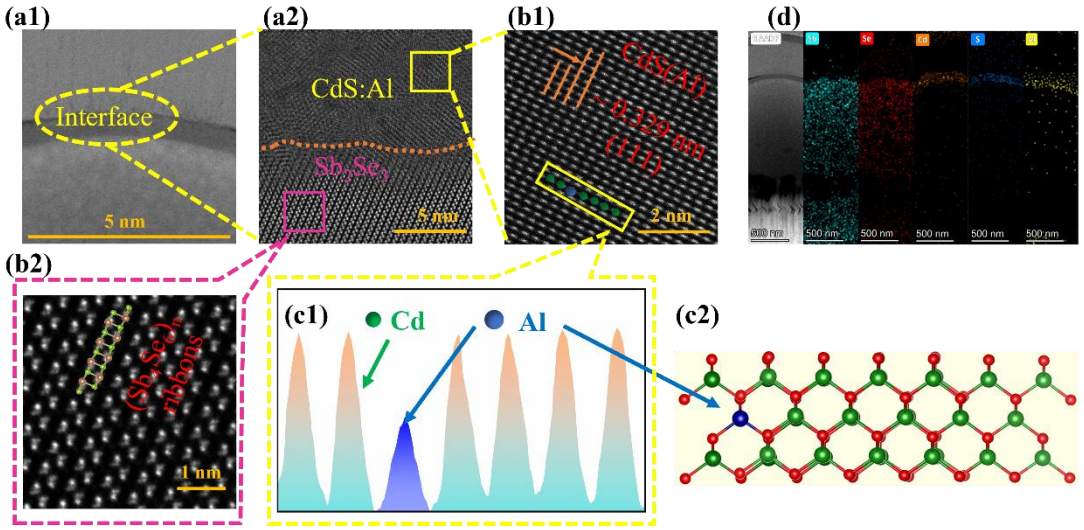

Figure 2. TEM characterization of the champion Sb_2Se_3/CdS:Al device. (a1) Cross-section TEM image of the Sb_2Se_3/CdS:Al heterojunction interface. (a2) HRTEM image of the heterojunction interface. HAADF-STEM image taken from CdS:Al buffer layer (b1) and Sb_2Se_3 absorber layer (b2). (c1) The intensity profiles of the HAADF signals obtained from the marked yellow rectangular frame in Figure 2b1. (c2) the corresponding atomic configuration of CdS:Al buffer layer. (d) The EDS elements mapping of Sb_2Se_3/CdS:Al heterojunction interface, including of Sb, Se, Cd, S, and Al.

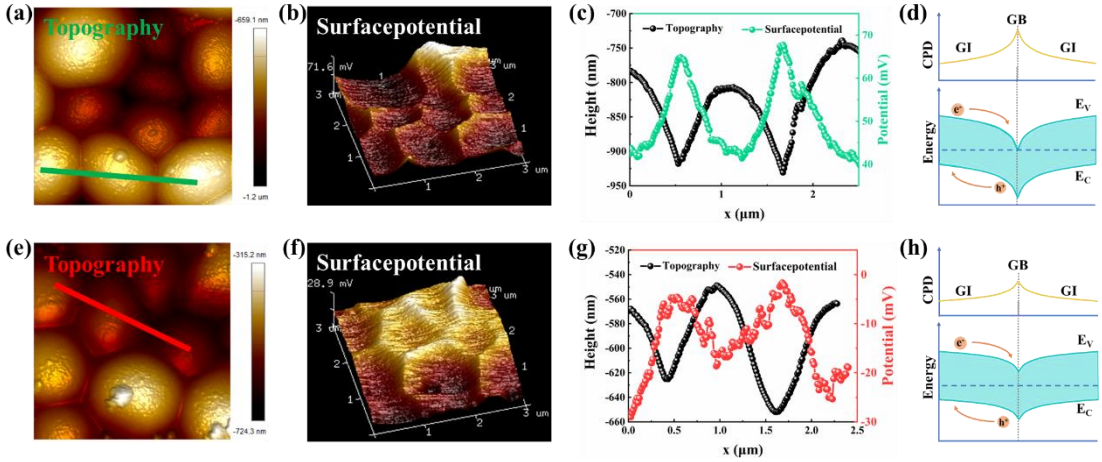

Figure 3. KPFM analysis of the representative pristine CdS (A0) and Al-doped CdS (A3) samples. (a), (e) Topography. (b), (f) Surface potential differences. (c), (g) Topography and Surface potential line profile (acquired from scanning the green line in (a) and (b)) for pristine CdS and Al-doped CdS thin film. (d), (h) The schematic diagrams corresponding to KPFM results.

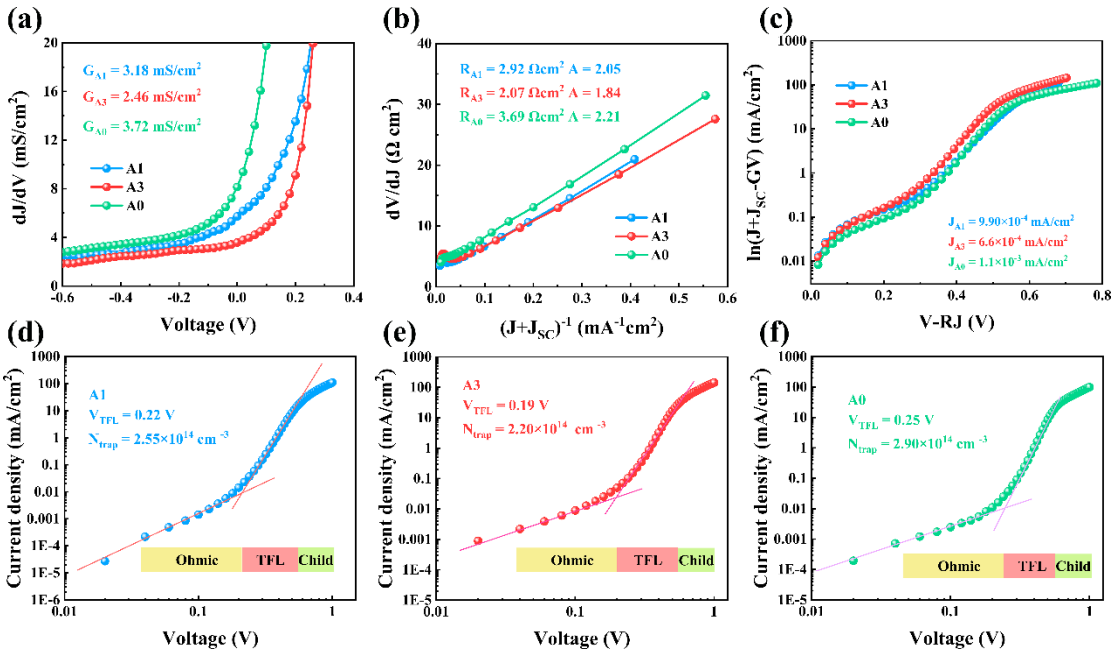

Figure 4. Dark *J–V* electrical behaviors of the representative A1, A3, and A0 device. (a) Shunt conductance *G* characterizations. (b) Series resistance *R* and ideality factor *A* characterizations. (c) Reverse saturation current density J_0 characterizations. (d-f) Logarithmic *J–V* curves of the A1, A3, and A0 devices, respectively.

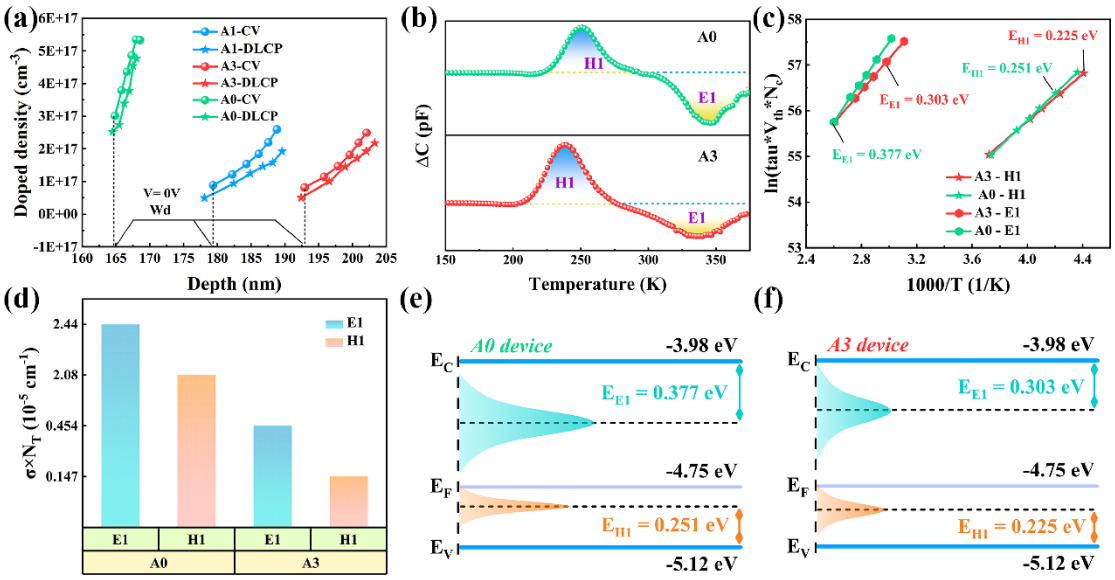

Figure 5. (a) *C–V* and DLCP profiling. (b) DLTS signals from pristine CdS A0 and Al-doped CdS A3 devices. (c) Arrhenius plots obtained from DLTS signals. (d) Histogram of the calculated $\sigma \times N_T$ values of traps in Sb_2Se_3 devices. Schematic diagram of defects in A0 (e) and A3 (f) device.

Table 2. Doping density calculated from *C–V* and DLCP profiling of the A1, A3 and A0 devices.

Devices	W_d (nm)	N_{CV} (cm^{-3})	N_{DLCP} (cm^{-3})	N_i (cm^{-3})
A1	179	8.90×10^{16}	4.97×10^{16}	3.93×10^{16}
A3	193	8.16×10^{16}	5.08×10^{16}	3.08×10^{16}
A0	165	3.01×10^{17}	2.50×10^{17}	4.90×10^{16}

Table 3. Defect characteristics of the A3 and A0 devices.

Devices	Defect	E_T (eV)	N_T (cm^{-3})	σ (cm^2)	$N_T\times\sigma$ (cm^{-1})
A3	E1	E_C – 0.225eV	2.28×10^{14}	1.98×10^{-20}	4.54×10^{-6}
	H1	E_V + 0.303 eV	2.50×10^{14}	5.88×10^{-21}	1.47×10^{-6}
A0	E1	E_C – 0.251eV	3.73×10^{14}	6.56×10^{-20}	2.44×10^{-5}
	H1	E_V + 0.377 eV	4.57×10^{14}	4.55×10^{-20}	2.08×10^{-5}

Table of contents: An effective strategy of Al^{3+} cation doping on CdS buffer layer was introduced in Sb_2Se_3 solar cells. The optimized band alignment, suppressed interface recombination, and enhanced carrier transport, result in the improvement of device performance. Consequently, the champion Sb_2Se_3/CdS:Al device delivers interesting PCE of 8.41%, accompanied with significant increase of J_{SC} to 28.26 mA/cm^2 as compared to the un-doped counterpart.

ToC figure

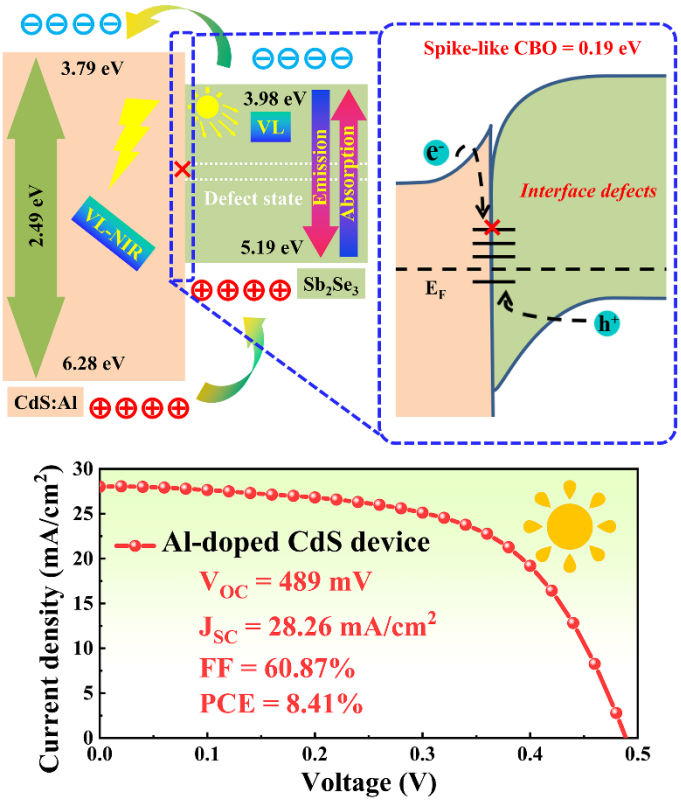

Supporting Information

Carrier Transport Enhancement Mechanism in Highly Efficient Antimony Selenide Thin-Film Solar Cell

Yandi Luo, Guojie Chen, Shuo Chen, Nafees Ahmad, Muhammad Azam, Zhuanghao Zheng, Zhenghua Su, Michel Cathelinaud, Hongli Ma, Zhigang Chen, Ping Fan, Xianghua Zhang, and Guangxing Liang**

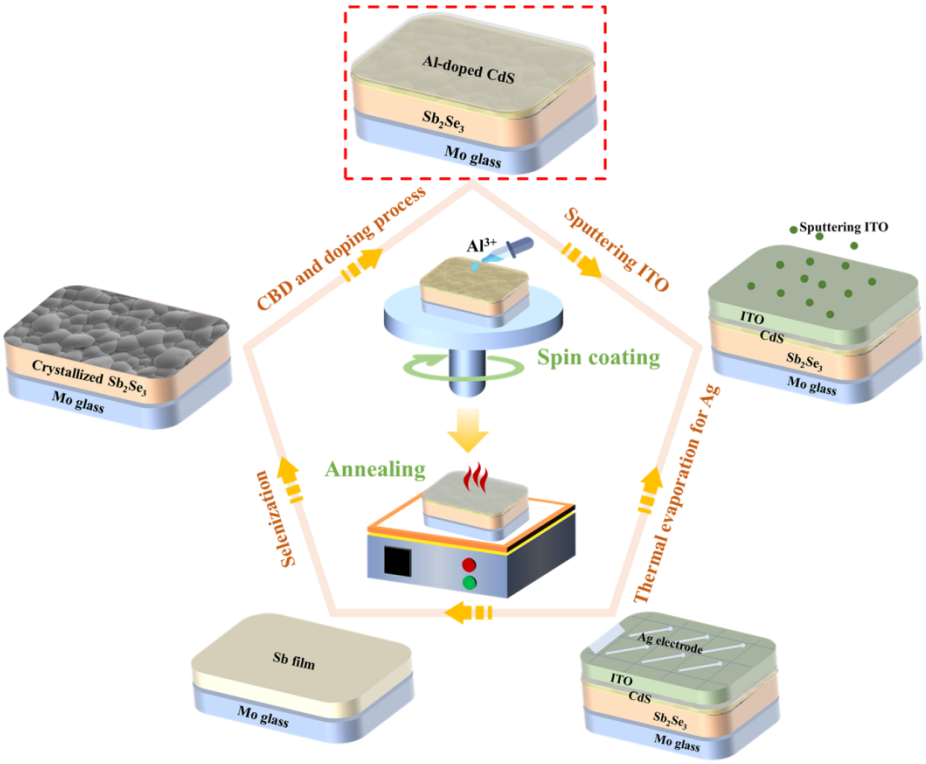

Figure S1. The schematic illustration of the fabrication processes for the substrate structured Sb_2Se_3 solar cell, and the schematic illustration of the Al-doped CdS film deposition using spin coating and annealing process is depicted at the center.

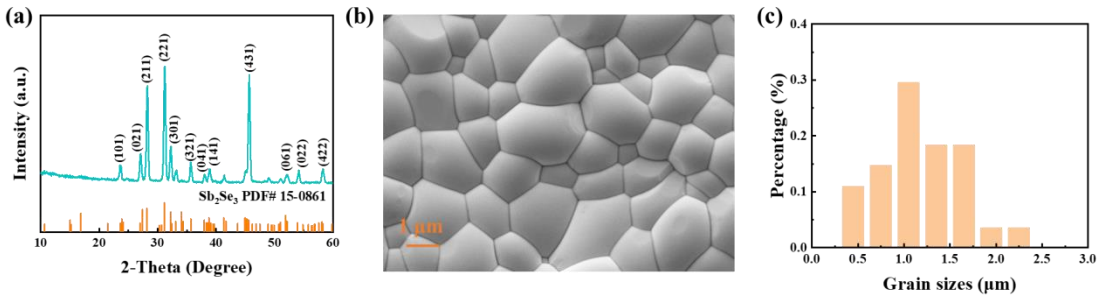

Figure S2. (a) XRD patterns, (b) SEM top-view images and (c) Grain size distributions of the Sb_2Se_3 thin films.

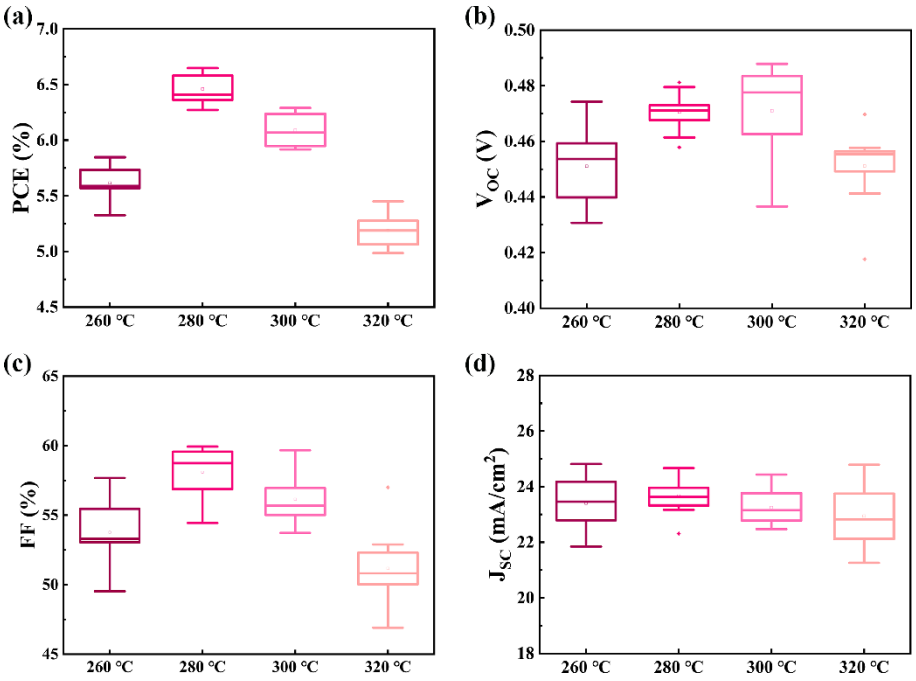

Figure S3. Statistical boxplots of (a) PCE; (b) V_{OC}; (c) FF; (d) J_{SC} for Sb_2Se_3 solar cells based on Al-doped CdS buffer layer as a function of annealing temperatures. The edges of the box represent the 25th and 75th percentile; the whisker length defines the upper inner and lower inner fence values; the line in the middle of the box marks out the median value, and the crosses the minimum and maximum values.

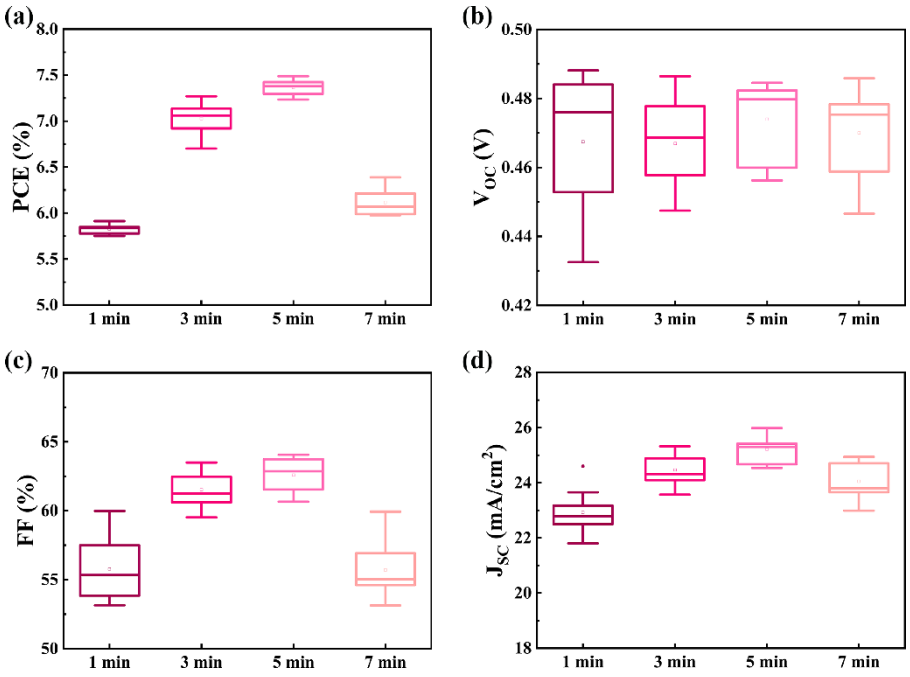

Figure S4. Statistical boxplots of (a) PCE; (b) V_{OC}; (c) FF; (d) J_{SC} for Sb_2Se_3 solar cells based on Al-doped CdS buffer layer as a function of annealing durations.

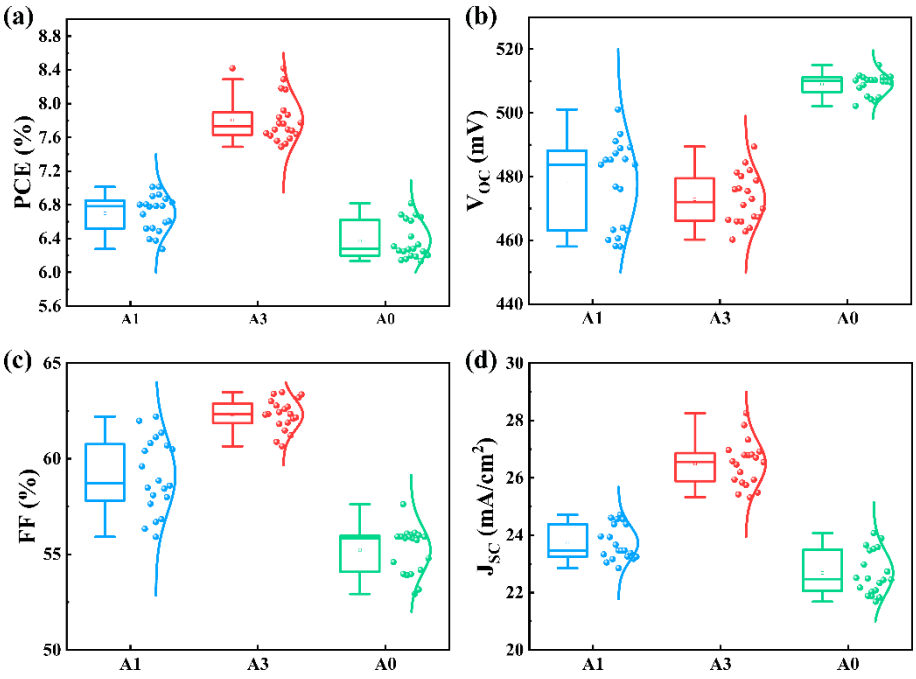

Figure S5. Statistical box-plots of (a) PCE; (b) V_{OC}; (c) FF; (d) J_{SC} for the representative A1, A3, and A0 Sb_2Se_3 solar cells.

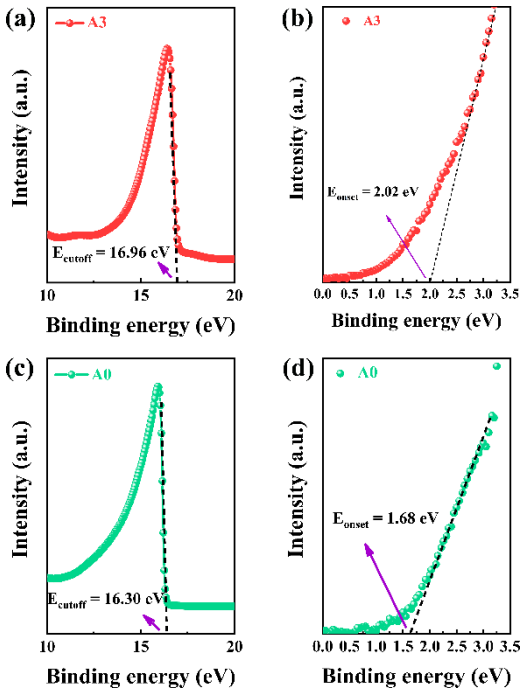

Figure S6. UPS characterizations of A3 (a) and A0 (b) thin films. Schematic diagram of defects in pure CdS (c) and Al-doped CdS (d) devices.

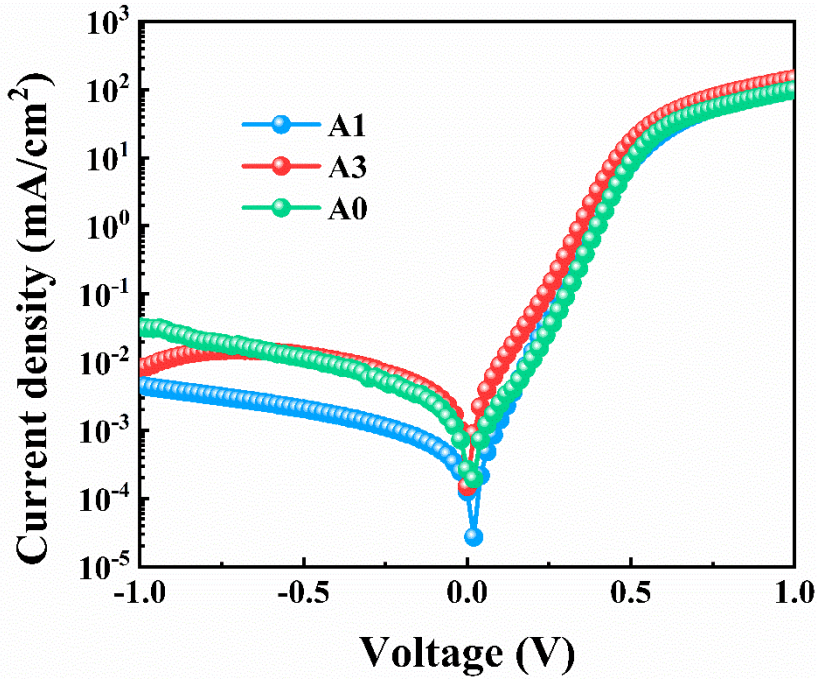

Figure S7. Dark *J–V* curves of the representative A1, A3, and A0 device.

Table S1. Electrical properties for the pristine CdS and Al-doped CdS buffer layer based Sb_2Se_3 solar cells.

Devices	*G* (mS/cm^2)	R_S (Ω cm^2)	*A*	J_0 (mA/cm^2)
A1	3.18	2.93	2.05	9.9×10^{-4}
A3	2.46	2.07	1.84	6.6×10^{-4}
A0	3.72	3.69	2.21	1.1×10^{-3}

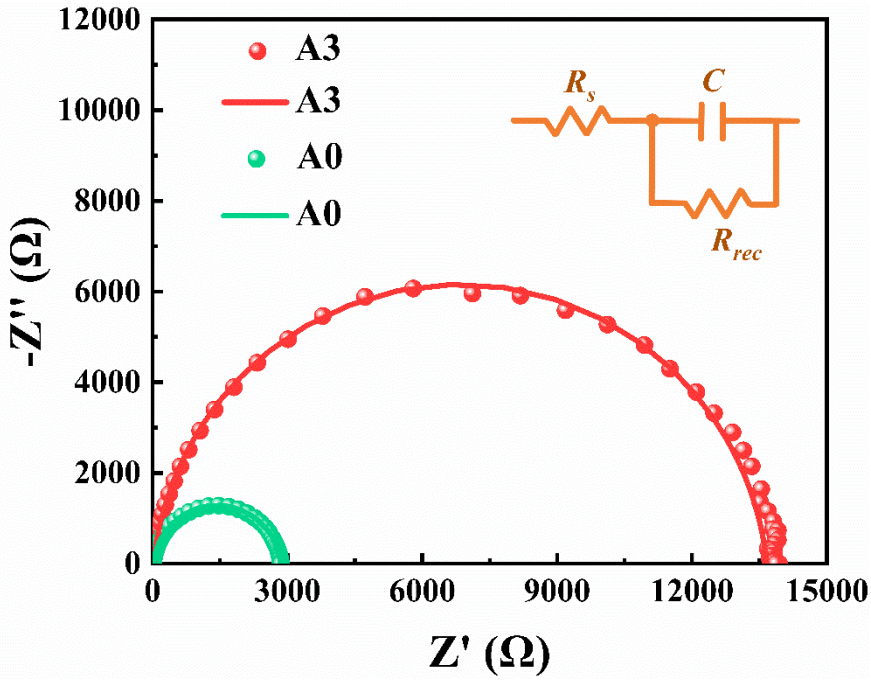

Figure S8. Nyquist plots of the impedance for A0 device and A3 device (inset equivalent circuit employed to fit the Nyquist plots), experimental data are shown as dotted circles and the fitted results are shown as solid lines.